The Astrophysical Journal, 875:27 (8pp), 2019 April 10 https://doi.org/10.3847/1538-4357/ab0e01

The Sequence of Coronene Hydrogenation Revealed by Gas-phase IR Spectroscopy

Stephanie Cazaux[1,2], Yann Arribard[3], Dmitrii Egorov[3], Julianna Palotás[4], Ronnie Hoekstra[3], Giel Berden[4], Jos Oomens[4], and Thomas Schlathölter[3]
[1] Faculty of Aerospace Engineering, Delft University of Technology, Kluyverweg 1, 2629 HS, Delft, The Netherlands
[2] University of Leiden, P.O. Box 9513, 2300 RA, Leiden, The Netherlands
[3] Zernike Institute for Advanced Materials, University of Groningen, Nijenborgh 4, 9747AG Groningen, The Netherlands; t.a.schlatholter@rug.nl
[4] FELIX Laboratory, Institute for Molecules and Materials, Radboud University, Toernooiveld 7, 6525 ED Nijmegen, The Netherlands
Received 2019 February 12; revised 2019 March 6; accepted 2019 March 6; published 2019 April 10

Abstract

Gas-phase coronene cations ($C_{24}H_{12}^{+}$) can be sequentially hydrogenated with up to 24 additional H atoms, inducing a gradual transition from a planar, aromatic molecule toward a corrugated, aliphatic species. The mass spectra of hydrogenated coronene cations $[C_{24}H_{12+n_H}]^{+}$ show that molecules with odd numbers of additional hydrogen atoms (n_H) are dominant, with particularly high relative intensity for "magic numbers" $n_H = 5$, 11, and 17, for which hydrogen atoms have the highest binding energies. Reaction barriers and binding energies strongly affect the hydrogenation sequence and its site specificity. In this contribution, we monitor this sequence experimentally by the evolution of infrared multiple-photon dissociation (IRMPD) spectra of gaseous $[C_{24}H_{12+n_H}]^{+}$ with $n_H = 3$–11, obtained using an infrared free electron laser coupled to a Fourier transform ion cyclotron mass spectrometer. For weakly hydrogenated systems ($n_H = 3$, 5) multiple-photon absorption mainly leads to loss of H atoms (and/or H_2). With increasing n_H, C_2H_2 loss becomes more relevant. For $n_H = 9$, 11, the carbon skeleton is substantially weakened and fragmentation is distributed over a large number of channels. A comparison of our IRMPD spectra with density functional theory calculations clearly shows that only one or two hydrogenation isomers contribute to each n_H. This confirms the concept of hydrogenation occurring along very specific sequences. Moreover, the atomic sites participating in the first 11 steps of this hydrogenation sequence are clearly identified.

Key words: astrochemistry – ISM: lines and bands – methods: laboratory: molecular – molecular processes – techniques: spectroscopic

1. Introduction

A large number of galactic and extragalactic sources feature infrared emission bands at very specific wavelengths that are referred to as the aromatic infrared bands (AIBs). Even though an unambiguous assignment of individual molecular species to the AIBs is still lacking, it is generally believed that these bands are due to infrared emission from the class of polycyclic aromatic hydrocarbon molecules (PAHs; Leger & Puget 1984; Allamandola et al. 1985). These PAHs may be neutral or ionized (Bauschlicher 1998; Oomens et al. 2001), mostly aromatic (Li & Draine 2012), and possibly partially hydrogenated (Snow et al. 1998). Major bands consistent with CC and CH vibrations are commonly observed around 3.3, 6.2, 7.7, 8.6, and 11.3 μm (Leger & Puget 1984; Allamandola et al. 1989), but details of the spectrum indicate that they may in part originate from more complex PAH derivatives (Tielens 2008). While identifying AIBs is currently impossible due to the large number of candidate PAH molecules, the bands can be assigned to families of PAHs. In addition the dominant aromatic C–C and C–H vibrational modes observed in the 6–15 μm region [3], there are features at 3.4, 3.47, 3.51, and 3.56 μm that appear together with the 3.3 μm aromatic band. These features point to a subset of the PAH population being decorated either with extra H atom(s) (Geballe et al. 1994; Snow et al. 1998; Li & Draine 2012; Thrower et al. 2012; Cazaux et al. 2016; Mackie et al. 2018; Maltseva et al. 2018) or with aliphatic groups (Joblin et al. 1996). Current databases contain (theoretical) infrared spectra for entire families of PAHs and their derivatives in different charge states, which are used, for instance, for quantitative determinations of PAH ionization fractions and aromaticity from observational data (Pilleri et al. 2012; Rosenberg et al. 2014; Boersma et al. 2015). In this way, PAH features serve as a probe of physical and chemical conditions in the near and distant universe. Understanding the kinetics of the hydrogenation of PAHs, as well as which hydrogenated PAHs are the most stable in different regions of the interstellar medium (ISM), are key to enabling adequate identification of PAH families in space.

PAHs are believed to account for about 20% of the carbon available in the galaxy (Joblin et al. 1992), therefore they likely play an important role in different processes in the ISM. In particular, PAHs are thought to be important catalysts for the formation of molecular hydrogen, the most abundant molecule in the universe (Habart et al. 2004; Mennella et al. 2012; Thrower et al. 2012; Boschman et al. 2015). The presence of pre-adsorbed H atoms on PAHs increases the yield of H_2 formation by many orders of magnitude, rendering this process an important route toward molecular hydrogen formation in the ISM (Bauschlicher 1998; Mennella et al. 2012; Boschman et al. 2015; Foley et al. 2018).

In a previous study (Cazaux et al. 2016), we showed by a combination of experiments and theory that hydrogenation of coronene cations ($C_{24}H_{12}^{+}$) follows a sequence guided by binding energies and reaction barriers. This sequence implies that coronene cations with an additional 5, 11 and 17 H atoms (highest binding energy and large barrier for addition of the next H atom) are the most abundant hydrogenation states in experimental mass spectra. In the present study, we use IR spectroscopy to identify the structure of different hydrogenation stages of coronene cations. We confirm that hydrogenation proceeds along a well-defined sequence of atomic sites. The sequence of PAH hydrogenation leading to superhydrogenated

PAHs is crucial for the search of hydrogenated PAHs, as well as the formation of H_2 in space.

2. Experimental and Theoretical Methods

IR spectra of gaseous hydrogenated coronene ions are recorded by infrared multiple-photon dissociation (IRMPD) spectroscopy in the Fourier Transform ion cyclotron resonance (FTICR) mass spectrometer coupled to the FELIX free electron laser (Oepts et al. 1995); this instrumentation has been described in detail elsewhere (Valle et al. 2005; Rijs & Oomens 2015).

2.1. Ion Generation

Coronene radical cations ($C_{24}H_{12}^+$), as well as protonated coronene ($C_{24}H_{13}^+$), are generated by electrospray ionization (ESI) using a Waters Z-Spray source (Knorke et al. 2009). The ESI solution consists of (65%) a saturated coronene solution in methanol, (30%) methanol, and (5%) a 10 mM $AgNO_3$ solution in methanol. Ions are accumulated in a linear rf hexapole ion trap mounted in a vacuum chamber maintained at a pressure of about 3×10^{-3} mbar by a 220 l/s turbomolecular pump. An atomic hydrogen source is connected onto this vacuum chamber via a small KF16 flange. A Slevin-type RF-discharge source (Slevin & Stirling 1981), originally used in crossed beam experiments (Hoekstra et al. 1991; Bliek et al. 1998), was used to generate a thermal beam of neutral hydrogen atoms. Hydrogen atoms effuse continuously toward the protonated coronene ions in the accumulation hexapole through a small teflon tube reaching to just above the center of the hexapole rods. Due to collisions with the teflon tubing, which is at room temperature, the H atoms have thermal energies of about 25 meV. The hydrogen flux is controlled by tuning of the molecular hydrogen flow to the discharge source. The ions are continuously injected from the ESI source into the accumulation hexapole, where they are exposed to a continuous beam of atomic hydrogen. The precursor coronene radical cations can be considered to be at internal temperatures of about 300K. However, upon a single H attachment, the binding energy (typically 2–3 eV) is deposited into the system, leading to strongly elevated internal temperatures that subsequently decrease again, due to, for instance, IR emission.

2.2. IRMPD Spectroscopy

The contents of the hexapole trap are then pulse-extracted and sent to the ICR cell via a quadrupole bender and a 1 m long RF octopole ion guide. A typical mass spectrum recorded in our FTICR-MS resolves the series coronene ions with different degrees of hydrogenation, as shown in Figure 1. A stored waveform inverse Fourier transform (SWIFT; Guan & Marshall 1996) pulse applied to the two excitation electrodes of the ICR cell is used to mass-isolate a single hydrogenation state. Subsequently, these isolated ions are irradiated by typically 50 macropulses from FELIX (at a 10 Hz repetition rate). In addition to the precursor ion peak, a mass spectrum recorded after the irradiation shows new mass peaks due to IR-induced fragments whenever the laser frequency is in resonance with an IR absorption band of the ion. We determine the fragmentation yield as the ratio of the intensity of all fragment peaks over the intensity of the fragment plus precursor ion peaks. This yield value is then plotted versus IR frequency for a series of mass spectra recorded while scanning the wavelength of FELIX. When fragmentation is

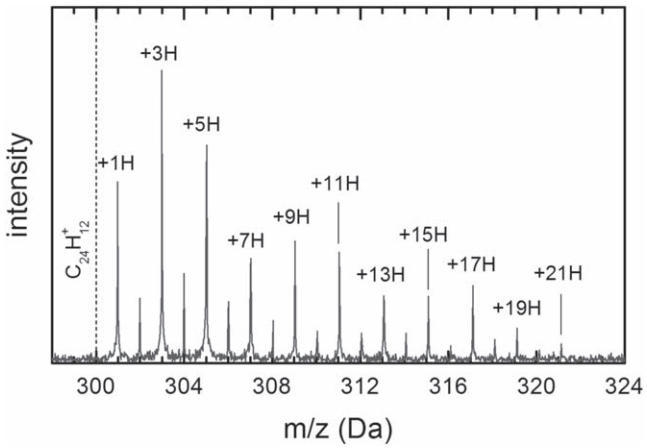

Figure 1. Typical mass spectrum of hydrogenated coronene cations ($[C_{24}H_{12}+n_H]^+$) before mass isolation in the FTICR mass spectrometer.

distributed over a large number of dissociation channels, the individual fragment mass peaks may be too weak for quantitative analysis. In such cases, the IR spectrum is derived from the IR-induced decrease of the precursor ion alone. Note that the resulting IRMPD spectrum is more sensitive to fluctuations in the ion current during the irradiation. FELIX macropulse energies amount to about 50 mJ, with somewhat lower values toward the high-frequency end of the scan range. The yield is linearly corrected for changing pulse energies. The FELIX wavelength is calibrated online using a grating spectrometer to an accuracy of about ± 2 cm^{-1}. The bandwidth of the radiation is less than 1% of the central frequency.

2.3. Hydrogenation States Produced

As a general rule (Cazaux et al. 2016), the heights of the reaction barriers for H attachment to $[C_{24}H_{12}+n_H]^+$ alternate with hydrogenation state n_H. For even n_H, attachment occurs either with small ($\sim$0.01 eV) or no barrier. For odd n_H, attachment involves a larger reaction barrier. Apparently, the closed shell hydrogenation states, which have an odd-number n_H, are stable while the radical species, which have an even-number n_H, are less stable. In Figure 1, this manifests as an odd/even intensity variation, with low intensities observed for even n_H (note that these mass peaks are mostly due to the approximate 20% presence of the ^{13}C-isotope of the adjacent odd n_H species). The "magic" hydrogenation states of particularly high binding energies (Cazaux et al. 2016) do not stand out in Figure 1 because the accumulation trap filling from the ESI source and atomic H exposure were done in parallel, washing out such effects.

2.4. Computational Methods

Equilibrium geometries and harmonic vibrational frequencies of the hydrogenated coronene $[C_{24}H_{12}+n_H]^+$ cations were calculated using density functional theory (DFT) as implemented in Gaussian 09 revision D01 (Frisch et al. 2009). The hybrid B3LYP functional was used with the 6-311+G(d, p) basis set, which is known for its superior performance, especially in predicting IR spectra. A scaling factor of 0.9679 was applied to the calculated harmonic frequencies, as well as a Gaussian convolution with a width (FWHM) of 30 cm^{-1}. Single-point energies were calculated at the MP2/6-311+G (2d, 2p) level of theory using the geometries optimized at the

B3LYP/6-311+G(d, p) level, to mitigate possible effects of dispersion on relative energies.

3. Results and Discussion

IRMPD spectroscopy is based upon the principle that only when the IR laser radiation is absorbed resonantly is energy deposited into the molecular ion. The energy is rapidly distributed over all nuclear degrees of freedom by intramolecular vibrational redistribution. When the dissociation threshold is exceeded, statistical dissociation occurs along the pathways with the lowest energies of activation, resulting in the respective dissociation products appearing in the mass spectrum. Here, we perform IRMPD measurements of individual $[C_{24}H_{12}+n_H]^+$ ions as a function of the number of attached hydrogen atoms n_H.

Each added hydrogen atom reduces the aromaticity of the molecular ion and increases its aliphatic character. This leads to substantial changes in the HOMO-LUMO gap (Pathak & Sarre 2008; Hammonds et al. 2009) and to a transition from a planar to a puckered geometry (Cazaux et al. 2016). These electronic and structural changes influence the stability of the molecular ions. The actual degree of stability of the ions has been debated. On the one hand, the added H atoms may drive the loss of molecular hydrogen, but on the other hand, the weakening of the aromatic carbon skeleton induced by hydrogenation may lead to CC bond cleavages rather than H_2-expulsion. For instance, under conditions of IRMPD, protonated dihydro-naphthalene undergoes H_2-loss (Vala et al. 2009), whereas protonated tetrahydro-naphthalene does not produce H or H_2 at all, but only shows breakup of the carbon frame (Vala et al. 2017).

Various other experiments involving different methods of PAH activation have shown the same ambivalence of dissociation pathways. For instance, for superhydrogenated neutral pyrene molecules, a weakening effect was observed. Here, fragmentation involving C-backbone rupture was found to be the highest decay channel, both in collision and in photoionization studies (Gatchell et al. 2015; Wolf et al. 2016). For coronene, Reitsma et al. (2014) have shown that the attachment of multiple hydrogen atoms to the cation strongly influences the molecular response upon core ionization by soft X-rays, whereas the coronene radical cation $[C_{24}H_{12}]^+$ undergoes predominantly H- and H_2- loss, leading to underhydrogenated species, for superhydrogenated species $[C_{24}H_{12+n_H}]^+$ facile loss of the extra hydrogen atoms is observed, resulting in the same product ions (Reitsma et al. 2014, 2015). Loss of C-containing fragments was not observed in these experiments, studying species with n_H up to 9.

3.1. Mass Spectra: IR-induced Fragmentation

The implications of IRMPD on the systems under study here are shown in Figure 2. From the top to bottom panels, IRMPD mass spectra for $[C_{24}H_{12}+n_H]^+$ with $n_H = 3$–11 are displayed. The IR wavelength was tuned to the C–C stretch at around 6.3 μm, because this vibrational transition is strong for all hydrogenated ions under study. For each species, a reference mass spectrum with the laser off-resonance is displayed for comparison. The main observations are as follows:

1. $n_H = 3$. Mostly loss of two and three H atoms is observed, resulting in the coronene radical cation and protonated coronene. The very weak peaks at lower masses are present in both resonant and non-resonant mass spectra and are therefore attributed to artifacts and/or contaminants.
2. $n_H = 5$. The mass spectrum again shows prominent peaks due to the coronene radical cation and protonated coronene, indicating the loss of five and four hydrogen atoms, respectively. In addition, a clear peak at $m/z = 276$ is observed, which is due to a mass loss corresponding to C_2H_5. Since C_2H_2 loss is common in PAH fragmentation, this channel may be due to sequential loss of C_2H_2 and three H atoms. Somewhat less intense, a peak at $m/z = 277$ appears. In analogy, this peak may be due to a sequential loss of two H atoms (or H_2) and C_2H_2. Similar processes have been previously described by Rapacioli et al. (2018).
3. $n_H = 7$. Loss of six and seven hydrogen atoms producing the coronene cation and protonated coronene is of comparable intensity to the C_2H_7 loss channel. Again, loss of C_2H_2 plus four and five H atoms, which occurs at similar intensities, is most likely.

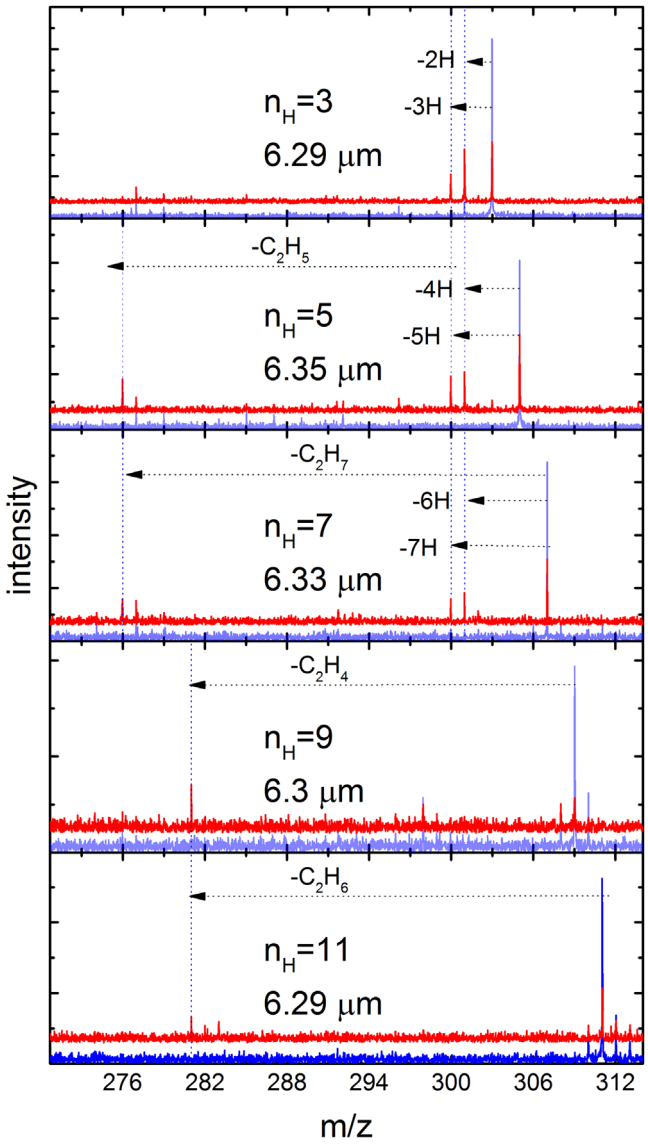

Figure 2. Red: mass spectra for resonant IRMPD at about 6.3 μm (C–C stretch) and $n_H = 3$–11. Blue: off-resonance reference spectrum.

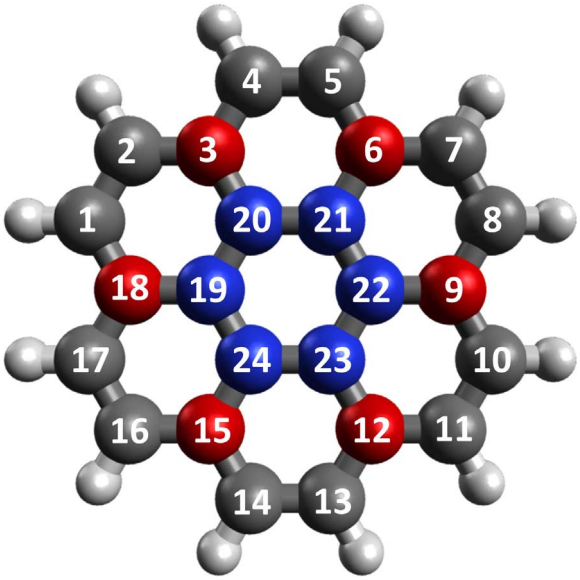

Figure 3. Structure of the coronene cations with the numbering convention used in this article. Outer-edge carbon atoms are shaded gray, inner-edge carbon atoms are in red, and center ring atoms are in blue.

4. $n_H = 9$. Here, the dissociation behavior deviates strongly from those above for $n_H = 3$, 5, and 7. No signatures of the coronene cation and protonated coronene created by the loss of only hydrogen are observed. A weak C_2H_4 loss channel into a fragment with $m/z = 281$ is evident. Smaller fragments are difficult to distinguish from the background. Since the fragmentation is likely distributed over many weak channels, IRMPD spectra were derived from IR-induced depletion of the precursor ion mass peak only.
5. $n_H = 11$. The situation is analogous to what is observed for $n_H = 9$, with the exception that the $m/z = 281$ fragment is now due to a mass loss corresponding to C_2H_6, and it is relatively weaker. This might be a signature of sequential loss of C_2H_4 plus two H atoms, since peaks at $m/z = 282$ (mass loss corresponding to C_2H_4 plus one H atom) and $m/z = 283$ (C_2H_4 mass loss) are also present.

The data displayed in Figure 2 thus demonstrate the existence of a low-n_H regime (up to $n_H = 7$) in which photodissociation primarily produces the coronene radical cation ($m/z = 300$) or protonated coronene ($m/z = 301$). In this regime, superhydrogenation protects the integrity of the PAH cation, as also observed previously by Reitsma et al. (2014). For $n_H \geqslant 9$ the structural weakening of the carbon skeleton becomes relevant and hardly any intact coronene radical cations are observed anymore, in line with conclusions of Gatchell et al. (2015).

3.2. IRMPD of Hydrogenated Coronene Cations: Following the Sequence

Figure 3 shows the structure of coronene without extra hydrogen and indicates the numbering of C-atoms used in this article. The theoretically predicted hydrogenation sites as a function of degree of superhydrogenation n_H from Cazaux et al. (2016) are given in Table 1 for $n_H = 3$–11. Hydrogenation proceeds via sites in relatively close vicinity to each other, because an attached hydrogen atom locally disturbs the geometric and electronic structure. This facilitates a near-neighbor addition of the next hydrogen atom. Hydrogenation up to $n_H = 11$ therefore strongly alters one side of the coronene cation, while leaving the other side largely unaffected. Using the IR spectra of the individual hydrogenation states, we verify the correctness of the predicted hydrogenation sequence.

Table 1
The Energetically Preferred Hydrogenated Sites for Different Degrees of Superhydrogenation n_H as Determined by Theoretical Simulations (Cazaux et al. 2016) and Determined by the IR Spectroscopy in This Work

n_H	Hydrogenated Sites Cazaux et al. (2016)	Hydrogenated Sites This Work
3	1 2 5	1 2 3
		1 2 5
5	1 2 3 4 5	1 2 3 4 5
7	1 2 3 4 5 7 8	1 2 3 4 5 10 11
9	1 2 3 4 5 6 7 8 11	1 2 3 4 5 6 7 8 11
		1 2 3 4 5 6 7 10 11
11	1 2 3 4 5 6 7 8 9 10 11	1 2 3 4 5 6 7 8 9 10 11

3.2.1. $n_H = 3$

The bottom panel of Figure 4 shows the experimental IRMPD spectrum for $n_H = 3$. The spectra show 5 peaks, centered at wavelengths around 6.3 μm (CC stretch), 7.43, 7.63, 8.32, 8.67 μm (CH in-plane bend), and 11.59 μm (CH out-of-plane bend), that can be clearly distinguished and are indicated by dashed lines. Energetically, it is very clear that the first hydrogen attachment involves an outer-edge site (see Figure 3). This attachment lowers the barrier for the attachment of a hydrogen atom to the adjacent outer-edge site. With sites 1 and 2 hydrogenated, the prediction for the third attachment is site 5 (Cazaux et al. 2016), so the lowest-energy isomer for $n_H = 3$ is (1 2 5).

Figure 4 also shows the IR spectra calculated for six different $n_H = 3$ configurations with Gibbs energy increasing from bottom to top (the energies are summarized in Table 2). Just above the IRMPD spectrum in Figure 4, the DFT-computed IR spectrum for the energetically most favorable isomer (1 2 5) is displayed, which is in good agreement with the experimental data. If the third atom is on the neighboring inner-edge site, (1 2 3), good agreement between DFT and IRMPD is observed as well, but the relative Gibbs-free energy is about 0.14 eV higher. Hydrogenation site 8 is similar to site 5, but one ring further away from sites 1 and 2. The DFT spectrum obtained for (1 2 8) is mostly similar to the IRMPD data, but lacks the peak at 8.32 μm. Putting the third hydrogen atom on the outer-edge site 4, which is closer to the first two hydrogen atoms, (1 2 4), a broad group of peaks between 7.4 and 6.3 μm appears that is not observed in the measurements. Also, for this sequence, the peak at 8.32 μm (CH in-plane bend) is missing.

The next panel depicts the IR absorption spectrum for the (1 2 9) configuration, i.e., another inner-edge site, but further away from the initial sites. Again, there is an additional peak between 7.4 and 6.3 and the 6.3 μm peak is shifted and split up in two. The topmost calculated spectrum corresponds to a sequence, involving an inner-ring site (1 2 20). Here, most peaks are shifted and again a peak between 7.4 μm (CH in-plane bend) and 6.3 μm (CC stretch) appears.

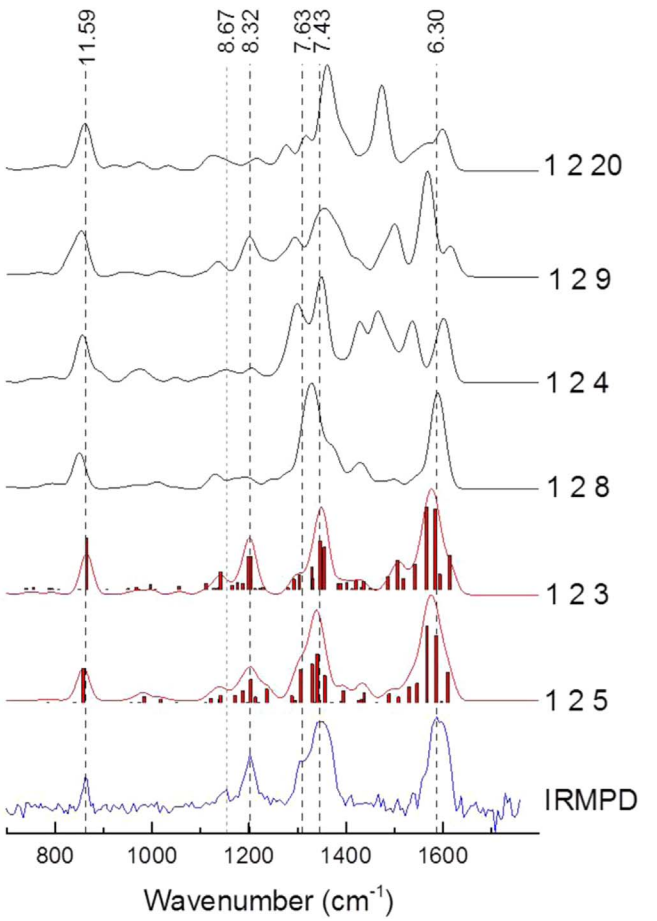

Figure 4. IR absorption spectra for $[C_{24}H_{12}+3H]^+$ computed by DFT at the B3LYP/6-311+G(d, p) level for six different sequences of hydrogen attachment. The sequences are given to the right of each spectrum. The bottom spectrum displays the measured IRMPD spectrum. The dashed lines indicate the experimentally observed peak maxima.

Table 2
Relative Gibbs-free Energies for Different Configurations of $[C_{24}H_{12}+3H]^+$ (in eV)

$n_H = 3$	B3LYP	MP2
1 2 5	0	0
1 2 3	0.1824	0.1412
1 2 8	0.4446	0.4495
1 2 4	0.5706	0.6011
1 2 9	0.9163	0.9264
1 2 20	0.9942	1.0031

Table 3
Relative Gibbs-free Energies for Different Configurations, $c_{n_H=5}$, of $[C_{24}H_{12}+5H]^+$ (in eV)

$n_H = 5$	B3LYP	MP2
1 2 3 4 5	0	0
1 2 3 7 8	0.7884	0.9143
1 2 4 5 8	0.8344	0.9950
1 2 4 7 8	0.8947	0.9643
1 2 4 5 7	1.3611	1.5713

As a conclusion, the IRMPD results for $n_H = 3$ confirm the predicted hydrogenation sequence (1 2 5), although the presence of the (1 2 3) sequence in the ion population cannot be excluded.

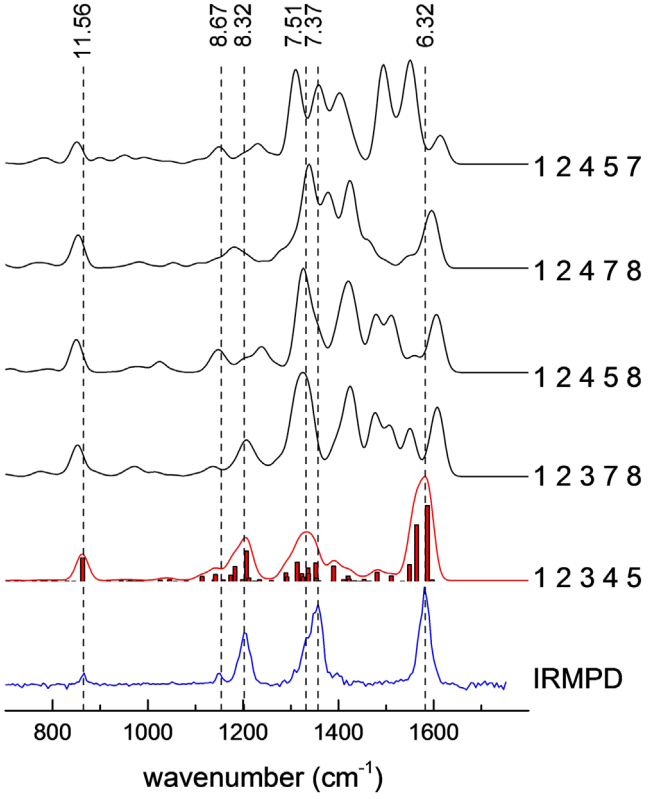

Figure 5. IR absorption spectra for $[C_{24}H_{12}+5H]^+$ computed by DFT at the B3LYP/6-311+G(d, p)): level for six different sequences of hydrogen attachment. The sequences are given to the right of each spectrum. The bottom spectrum displays the experimentally observed IRMPD spectrum. The dashed lines indicate experimentally observed peak positions.

3.2.2. $n_H = 5$

The bottom panel of Figure 5 displays the IRMPD data for $n_H = 5$. Qualitatively, the spectrum is very similar to the $n_H = 3$ case, with slightly shifted peak positions. The preferred hydrogenation sites as predicted by Cazaux et al. (2016) are (1 2 3 4 5). Here, calculated IR spectra for five hydrogenation isomers are displayed, with their Gibbs energies (see Table 3) increasing from bottom to top. The energetically most favorable configuration by far is (1 2 3 4 5) and its calculated spectrum is in excellent agreement with the experimental data. This configuration can be formed from the two most likely $n_H = 3$ isomers, (1 2 5) and (1 2 3), by the simple attachment of two additional H atoms.

Starting from (1 2 3) and placing the next two H atoms not on the outer-edge sites (4 5), but on (7 8), gives rise to (1 2 3 7 8), which is energetically much less favorable (+0.91 eV). The calculated IR spectrum features four strong peaks in the range between 7.4 and 6.3 μm that are not observed in the experiment. A similar result is obtained from the calculation for the outer-edge-only configuration (1 2 4 5 8), which may start out from (1 2 5) and add two H atoms to sites (4 8). The disagreement gets even worse for energetically higher, outer-edge-only configurations such as (1 2 4 7 8) and (1 2 4 5 7). The configuration (1 2 4 5 20) with two adjacent pairs of outer-edge sites and an inner-ring site does not seem to be stable and the corresponding calculations converge toward the (1 2 3 4 5) configuration. In conclusion, the IRMPD results for $n_H = 5$ confirm the predicted hydrogenation sequence (1 2 3 4 5). This configuration, $c_{n_H=5}$ = (1 2 3 4 5), is assumed as a basis for all

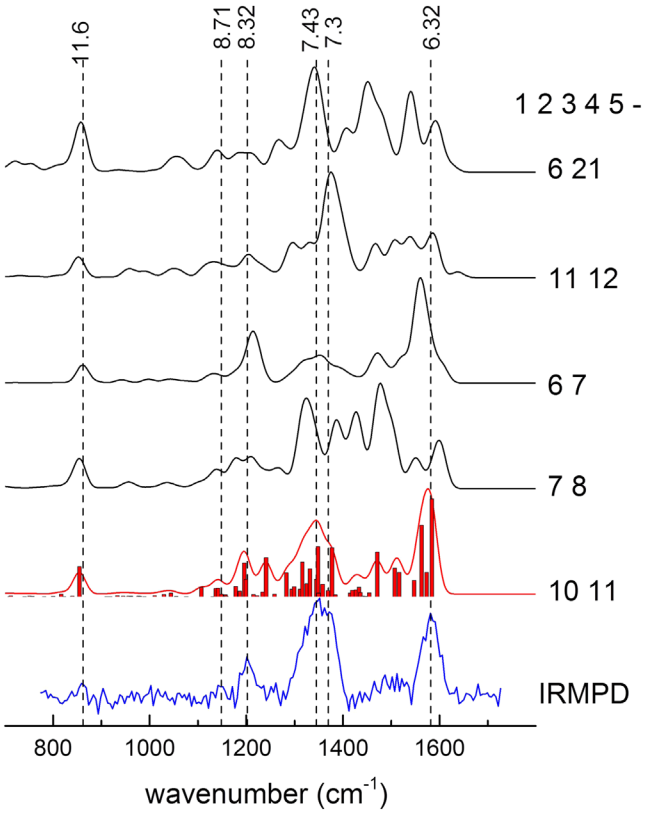

Figure 6. IR absorption spectra for $[C_{24}H_{12}+7H]^+$ computed at the B3LYP/6-311+G(d, p) level for different sequences of hydrogen attachment, given to the right of each panel. The experimentally observed IRMPD spectrum is displayed in the bottom panel.

higher hydrogenation states discussed below; other hydrogenation isomers for $n_H = 5$ can be confidently excluded based on the experimental data. Because of the remarkably high energetic difference between the most stable and the second most stable isomers, we have based the isomers investigated for $n_H > 5$ on the sequence (1 2 3 4 5).

3.2.3. $n_H = 7$

Figure 6 displays the experimental spectrum for $n_H = 7$ (bottom panel), with the spectra above showing the DFT results. The IRMPD spectrum remains similar to what is observed for $n_H = 3$ and $n_H = 5$, but with a broad, somewhat weaker feature between 7.4 and 6.3 μm.

Starting from the $c_{n_H=5}$ = (1 2 3 4 5) hydrogenation configuration, the predicted preferred hydrogenation sites are ($c_{n_H=5}$, 7 8), i.e., hydrogenation of the adjacent pair of outer-edge sites (Cazaux et al. 2016). According to the present calculations, the (7 8) pair of outer-edge sites is not hydrogenated; rather, the next-nearest pair of outer-edge sites (10 11) is (see Table 4). The energy difference between these two configurations is calculated to amount to 0.44 eV.

The calculated IR spectrum for ($c_{n_H=5}$ 10 11) is in good agreement with the IRMPD data. The computed IR spectrum for the ($c_{n_H=5}$ 7 8) configuration appears to deviate strongly from the experimental data: the CC stretch at 6.3 μm is reduced in intensity and instead, a series of strong peaks is predicted between 7.4 and 6.3 μm, disagreeing with the experimental observations. Moving an H atom from the outer-edge site (8) to the inner-edge site (6) gives rise to the ($c_{n_H=5}$ 6 7) configuration. The calculated spectral features peak at approximately correct positions but with much lower intensity for the broad CH in-plane bend modes at about 7.4 μm. Two additional $c_{n_H=5}$ based configurations at even higher relative energies have been investigated. Also, their calculated spectra disagree clearly with the IRMPD data, in particular for the ($c_{n_H=5}$, 6 21) configuration that features an inner-ring hydrogenation.

Table 4
Relative Gibbs-free Energies for the Lowest-energy Configurations of $[C_{24}H_{12}+7H]^+$ (in eV) Following the Addition of 2 H Atoms to the Ground Configuration of $[C_{24}H_{12}+5H]^+$, $c_{n_H=5}$ = (1 2 3 4 5)

H Sites		B3LYP	MP2
10	11	0	0
7	8	0.3757	0.4368
6	7	0.4762	0.5211
11	12	1.4274	1.5762
6	21	1.3039	1.3875

We conclude that the measured IRMPD spectrum for $n_H = 7$ disagrees with the hydrogenation sequence predicted previously ($c_{n_H=5}$, 7 8), but agrees with the energetically more favorable configuration ($c_{n_H=5}$, 10 11). This configuration is formed by the addition of two H atoms to from $c_{n_H=5}$ on outer-edge carbon sites, which are not on the adjacent ring but on the next-nearest ring.

3.2.4. $n_H = 9$

In the bottom panel of Figure 7 the experimental results for $n_H = 9$ are displayed. The IRMPD spectrum still has a very similar appearance, as observed for the lower hydrogenation states (although the main features are broadened). Two clear peaks become visible at 6.83 μm and at 6.57 μm.

The hydrogenation sites predicted by Cazaux et al. (2016) are ($c_{n_H=5}$ 6 7 8 11) and this configuration is also the energetically most favorable among the configurations investigated here (see Table 5). Since the hydrogenation configuration of $n_H = 7$ is determined as ($c_{n_H=5}$ 10 11), the predicted hydrogenation configuration for $n_H = 9$ cannot be formed by simple addition of two H atoms, but requires the rearrangement of at least one H atom. The comparison in Figure 7 suggests that the computed spectrum for this configuration reasonably reproduces the IRPMD spectrum, although the predicted shoulder on the low-wavelength side of the band 6.33 μm is not observed. Moreover, the intensities of the two bands at 6.83 μm and at 6.57 μm are somewhat off.

The IRMPD spectrum appears to agree approximately, as well with the next higher isomer ($c_{n_H=5}$ 6 7 10 11), which lies at about +0.1 eV from the lowest-energy configuration. It can be formed out of the minimum-energy hydrogenation configuration for $n_H = 7$ by simple addition of two H atoms.

The arrangement of all nine H atoms in a row along the PAH edge ($c_{n_H=5}$ 6 7 8 9) is slightly higher in energy, +0.26 eV, and the computed IR spectrum is in relatively poor agreement with the experimental data. The remaining three configurations investigated here, including one with inner-ring hydrogenation, are higher in energy and clearly exhibit spectra deviating from the IRMPD spectrum.

In conclusion, the limited quality of the IRMPD data, along with the relatively small energetic difference, do not allow us to clearly identify either ($c_{n_H=5}$ 6 7 10 11) or ($c_{n_H=5}$ 6 7 8 11).

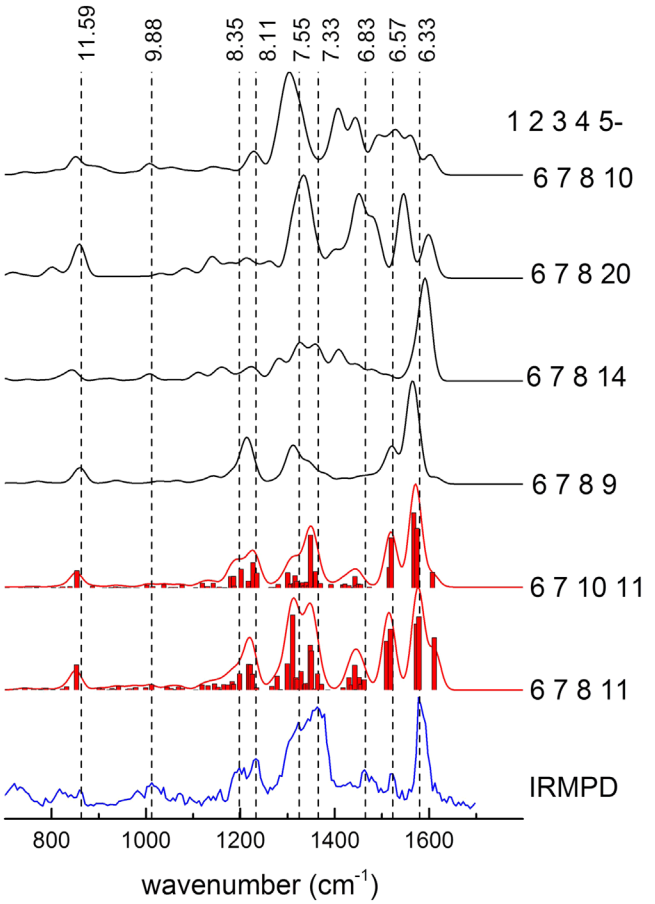

Figure 7. Computed IR absorption spectra for $[C_{24}H_{12}+9H]^+$ for different sequences of hydrogen attachment. The sequences are given to the right of each panel. The bottom spectrum displays the experimentally observed IRMPD spectrum.

Table 5
Relative Gibbs-free Energies of the Lowest-energy Hydrogenation Configurations of $[C_{24}H_{12}+9H]^+$ (in eV) for the Addition of 4 H Atoms to the Ground Configuration of $[C_{24}H_{12}+5H]^+$, $c_{n_H=5}$ = (12345)

H Sites				B3LYP	MP2
6	7	8	11	0	0
6	**7**	**10**	**11**	0.1012	0.0987
6	7	8	9	0.2614	0.2560
6	7	8	14	0.4083	0.4118
6	7	8	20	0.4367	0.4602
6	7	8	10	0.5587	0.5899

Note. The configuration in boldface can be formed from the ground configuration of $n_H = 7$ without any rearrangement of the first seven H atoms.

Note that ($c_{n_H=5}$ 6 7 10 11) can be formed directly from (1 2 3 4 5 10 11), which was identified as the most probable configuration for $n_H = 7$.

3.2.5. $n_H = 11$

Finally, the IRMPD spectrum for $n_H = 11$ is presented in Figure 8. The region between 6.3 and 8.7 μm slowly evolves into a continuum although some peaks are still recognizable. In Cazaux et al. (2016) the ($c_{n_H=5}$, 6 7 8 9 10 11) configuration is predicted and the present calculations confirm this (see Table 6). Moreover, this configuration can be formed both from the most likely and second most likely configurations of $n_H = 9$ without rearrangement of the first nine H atoms. The corresponding calculated IR spectrum resembles the IRMPD spectrum, although the limited resolution in the experimental spectrum does not allow for a firm conclusion. Nonetheless, the match with experiments appears to be better than that with any of the computed spectra for five other configurations shown in Figure 8. All these alternative configurations are based on the ($c_{n_H=5}$ 6 7 8) sequence, with the remaining three H atoms being attached to geometrically close sites or (in one case) to an inner ring site. Even the energetically lowest of these alternative configurations ($c_{n_H=5}$, 6 7 8 10 13 14) is +0.78 eV higher in

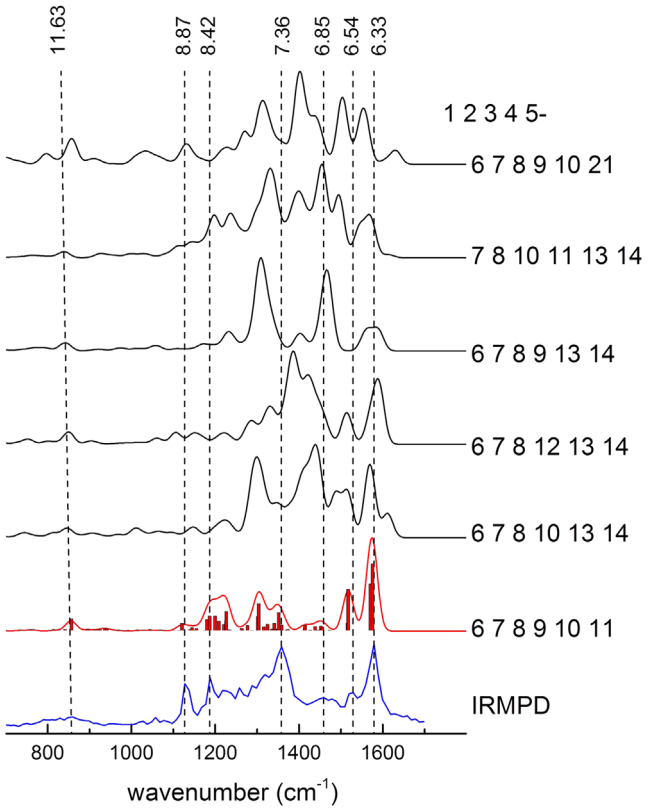

Figure 8. Computed IR absorption spectra for $[C_{24}H_{12}+11H]^+$ for six different sequences of hydrogen attachment. The bottom panel displays the experimentally observed IRMPD spectrum.

Table 6
Gibbs-free Energies of the Lowest-energy Hydrogenation Configurations of $[C_{24}H_{12}+11H]^+$ (in eV) for the Addition of 6 H Atoms to the Ground Configuration of $[C_{24}H_{12}+5H]^+$, $c_{n_H=5}$ = (1 2 3 4 5)

H Sites						B3LYP	MP2
6	**7**	**8**	**9**	**10**	**11**	0	0
6	7	8	10	13	14	0.6814	0.7764
6	7	8	12	13	14	0.7616	0.8076
6	7	8	9	13	14	0.8016	0.8872
7	8	10	11	13	14	1.1594	1.4297
6	7	8	9	10	21	1.6794	1.9196

Note. The configuration in boldface can be formed both from the most likely and second most likely configuration of $n_H = 9$ without rearrangement of the first nine H atoms. All other low-energy configurations require rearrangement of at least one of the initial nine H atoms.

energy (see Table 6). Its computed spectrum deviates substantially from the IRMPD data and this is even worse for the other configurations. This provides further support for ($c_{n_H=5}$, 6 7 8 9 10 11) being the preferred hydrogenation configuration for $n_H = 11$.

4. Conclusion

Previous computational studies have suggested that hydrogenation of cationic coronene occurs via a well-defined sequence in which hydrogen atoms become attached to preferential carbon sites until full hydrogenation is reached. This sequence, reported in Table 1, is governed by energetic barriers to hydrogen addition and binding energies, and produces hydrogenation states that are more abundant than others that are referred to as "magic numbers." In this study, we measured experimentally the IR absorption spectra of individual hydrogenated coronene cations with a well-defined number of additional H atoms (n_H). We compared the experimental IRMPD spectra with spectra predicted by DFT calculations. For each hydrogenation state studied ($n_H = 3$, $n_H = 5$, $n_H = 7$, $n_H = 9$, $n_H = 11$), we unambiguously determine that only one or two isomeric forms are present, as reported in Table 1. This confirms that hydrogenation is not a random process, but follows a precisely defined sequence.

The AIB infrared emission observed toward many astronomical objects contains, in addition to the main bands, various satellite features, including those appearing at 3.4, 3.47, 3.51, and 3.56 μm. These satellite features have often been suggested to be due to hydrogenated PAHs (Li & Draine 2012). In the present study we show that hydrogenated PAHs in specific isomeric forms are more abundant than others. Hence, only a few states could be populated, depending on the physical conditions determined by the kinetics of the H atom additions to PAHs driven by binding energies and reaction barriers. Looking for specific hydrogenation states of PAHs in the ISM could shed light on the different PAH families present, but also would constrain the physical conditions in different environments. Understanding the kinetics of H-addition and H-abstraction of PAHs is also crucial to addressing the role of PAHs as catalysts for the formation of H_2 in different zones within photodissociation regions (Habart et al. 2004). Deeper knowledge of PAH populations in different environments is thus essential to constraining the role PAHs have as proxies for physical conditions and for the formation of H_2 in space.

We gratefully acknowledge the Nederlandse Organisatie voor Wetenschappelijk Onderzoek (NWO) for the support of the FELIX Laboratory. This work is supported by the European MCSA ITN network "EUROPAH" (grant No. 722346) and the NWO Dutch Astrochemistry Network (DAN-II, grant No. 648.000.030). For the computational work, we acknowledge support by NWO under the "Rekentijd" program (grant No. 17603) and the SurfSARA staff.

ORCID iDs

Thomas Schlathölter https://orcid.org/0000-0001-9923-172X

References

Allamandola, L. J., Tielens, A. G. G. M., & Barker, J. 1985, ApJL, 290, L25
Allamandola, L. J., Tielens, A. G. G. M., & Barker, J. R. 1989, ApJS, 71, 733
Bauschlicher, C. W. 1998, ApJL, 509, L125
Bliek, F. W., Woestenenk, G. R., Hoekstra, R., & Morgenstern, R. 1998, PhRvA, 57, 221
Boersma, C., Bregman, J., & Allamandola, L. J. 2015, ApJ, 806, 121
Boschman, L., Cazaux, S., Spaans, M., Hoekstra, R., & Schlathölter, T. 2015, A&A, 579, A72
Cazaux, S., Boschman, L., Rougeau, N., et al. 2016, NatSR, 6, 19835
Foley, N., Cazaux, S., Egorov, D., et al. 2018, MNRAS, 479, 649
Frisch, M. J., Trucks, G. W., Schlegel, H. B., et al. 2009, Gaussian09 Revision E.01 (Wallingford, CT: Gaussian Inc.)
Gatchell, M., Stockett, M. H., de Ruette, N., et al. 2015, PhRvA, 92, 050702
Geballe, T. R., Joblin, C., D'Hendecourt, L. B., et al. 1994, ApJL, 434, L15
Guan, S., & Marshall, A. 1996, IJMSp, 157, 5
Habart, E., Boulanger, F., Verstraete, L., Walmsley, C. M., & Pineau des Forêts, G. 2004, A&A, 414, 531
Hammonds, M., Pathak, A., & Sarre, P. 2009, PCCP, 11, 4458
Hoekstra, R., de Heer, F. J., & Morgenstern, R. 1991, JPhB, 24, 4025
Joblin, C., Leger, A., & Martin, P. 1992, ApJ, 393, L79
Joblin, C., Tielens, A. G. G. M., Allamandola, L. J., & Geballe, T. R. 1996, ApJ, 458, 610
Knorke, H., Langer, J., Oomens, J., & Dopfer, O. 2009, ApJL, 706, L66
Leger, A., & Puget, J. L. 1984, A&A, 137, L5
Li, A., & Draine, B. T. 2012, ApJL, 760, L35
Mackie, C., Candian, A., Huang, X., et al. 2018, PCCP, 20, 1189
Maltseva, E., Mackie, C., Candian, A., et al. 2018, A&A, 610, A65
Mennella, V., Hornekær, L., Thrower, J., & Accolla, M. 2012, ApJL, 745, L2
Oepts, D., van der Meer, A., & van Amersfoort, P. 1995, Infrared Physics Technology, 36, 297
Oomens, J., Sartakov, B. G., Tielens, A. G. G. M., Meijer, G., & von Helden, G. 2001, ApJL, 560, L99
Pathak, A., & Sarre, P. J. 2008, MNRAS, 391, 110
Pilleri, P., Montillaud, J., Berné, O., & Joblin, C. 2012, A&A, 542, A69
Rapacioli, M., Cazaux, S., Foley, N., et al. 2018, PCCP, 20, 22427
Reitsma, G., Boschman, L., Deuzeman, M. J., et al. 2014, PhRvL, 113, 053002
Reitsma, G., Boschman, L., Deuzeman, M. J., et al. 2015, JChPh, 142, 024308
Rijs, A. M., & Oomens, J. 2015, Gas-Phase Ir Spectroscopy and Structure of Biological Molecules, 364 (Cham: Springer), 1
Rosenberg, M. J. F., Berne, O., & Boersma, C. 2014, A&A, 566, L4
Slevin, J., & Stirling, W. 1981, RScI, 52, 1780
Snow, T. P., Le Page, V., Keheyan, Y., & Bierbaum, V. M. 1998, Natur, 391, 259
Thrower, J. D., Jørgensen, B., Friis, E. E., et al. 2012, ApJ, 752, 3
Tielens, A. 2008, ARA&A, 46, 289
Vala, M., Oomens, J., & Berden, G. 2017, JPCA, 121, 4606
Vala, M., Szczepanski, J., Oomens, J., & Steill, J. 2009, JAChS, 131, 5784
Valle, J., Eyler, J., Oomens, J., et al. 2005, RScI, 76, 023103
Wolf, M., Giacomozzi, L., Gatchell, M., et al. 2016, EPJD, 70, 85